Ion beam joining of ceramic and carbon-based nanostructures

Das, P.; Möller, W.; Elliman, R. G.; Chatterjee, S.;

Originally published:

March 2021

Applied Surface Science 554(2021), 149616

DOI: https://doi.org/10.1016/j.apsusc.2021.149616

Perma-Link to Publication Repository of HZDR:

https://www.hzdr.de/publications/Publ-32493

Ion beam joining of ceramic and carbon-based nanostructures

Pritam Das[1], Wolfhard Möller[2], Robert Glen Elliman[3], Shyamal Chatterjee*[1]

[1]*School of Basic Sciences, Indian Institute of Technology Bhubaneswar, Jatni, Odisha, 752050, India*

[2]*Institute of Ion Beam Physics and Materials Research, Helmholtz-Zentrum Dresden-Rossendorf, 01328 Dresden, Germany*

[3]*Department of Electronic Materials Engineering, Research School of Physics and Engineering, Australian National University, Canberra, ACT 2601, Australia*

**Email: shyamal@iitbbs.ac.in*

Abstract

Ion beam assisted joining of nanostructured materials is a relatively new field. In particular ion beam technique has been proven to be worthwhile for joining ceramic nanostructures. However, a large scope is still remaining to study heterojunctions between two dissimilar materials as the process of formation of bonds between two dissimilar materials is still to be understood. In this work we pick up a ceramic oxide and carbon based material to study ion beam joining. Specifically, we for the first time show heterojunction formation between hydrogen titanate nanowire (HTNW) and carbon nanotube (CNT) by the low energy ion beam. In order to understand the mechanism, we have invoked density functional theory and three-dimensional ion-solid interaction simulations. Experimental results are supported by predictions of simulations and suggest that the joining is established through ion beam mixing, surface defects and sputter redeposition at the junction points. The current study enlightens how the defects and sputtered out atoms are involved in the joining process. The chemical bonds between HTNW and CNT are formed only when C vacancy and simultaneously non-lattice O and C were produced during irradiation. The effect of joining on electrical conductivity and surface wetting has also been studied experimentally in this work, which is supported by simulations.

Keywords: Welding; Ion irradiation; Heterojunction; TRI3DYN; Density functional theory; Transport property; Wetting

Introduction

The ability to manipulate and modify nanostructures has become increasingly important in fields such as photonics, optoelectronics, flexible electronics and micro- and nano-electromechanical systems [1]. Since nanowires and nanotubes offer many unique properties and can accommodate high stresses, they are particularly desirable building blocks. However, nanowire networks are generally poorly interconnected and suffer from problems such as poor mechanical strength and high contact resistance. The ability to join (or weld) such structures into integrated networks, therefore, has great potential for improving their functionality. Various methods have been employed to achieve such interconnectivity, including: cold welding, fusion welding, solid-state welding, diffusion bonding, soldering, mechanical bonding, and atomic diffusion. For example, Moreno-Moreno et al. joined two gold nanowires or silver nanowires by a cold-welding technique [2] and Seong et al. achieved fusion welding of two silver nanowires by exploiting their high contact resistance to locally melt the junction by Joule heating [3]. Polymer adhesive coatings have also been employed. For example, Kang et al joined silver nanowires using sodium halide salts [4]. Peng et al also creates bonding between Ag nanowires, which is formed by diffusion bonding in an acidic medium [5]. Soldering and using fastener materials is a modern method of nanowire joining. Using soldering and fastener materials method, various nanowires, such as silver [6], tin [7], germanium [8], silicon [9], zinc oxide [10,11], tin oxide [12] have been welded successfully.

Hydrogen titanate nanorods have been widely studied for unique properties and various potential applications in lithium-ion batteries, field emission, solar cells, hydrogen sensors, hydrogen storage, and active catalysts. [13–15] However, due to wide bandgap and limited conductivity,[16] hydrogen titanate exhibits poor battery performance, field emission, solar cells, and gas sensors. Whereas carbon nanotube is well known for its excellent electrical, optical, mechanical, and thermal properties. One of the possible ways to improve usefulness of hydrogen titanate could be by creating heterojunction between hydrogen titanate nanowires and carbon nanotubes. Several studies have been performed to create homojunction and heterojunction by different methods. Yao et al. used solution-based polyacrylonitrile for epitaxial welding of CNT.[17] The welded CNTs exhibit both high conductivity and high tensile strength. CNT is also used as a joining material between different layers by inserting between the polypropylene layers.[18] Jiang et al. welded two single-wall carbon nanotubes by graphitic carbon using the chemical vapor deposition method

and proposed to use them for fabricating transparent conductive films.[19] Tanaka et al. formed single-walled carbon nanotubes complexed with polyoxometalate and show the network's possible use in the development of neuromorphic devices based on neuroscience.[20] Similarly, Sang et al. created junctions between titanate nanotubes and TiO_2 nanoparticles by thermal annealing for photocatalytic application.[21] Hirose et al. made Au/Nb-doped strontium titanate Schottky junctions by RF magnetron sputtering and measured the current transport properties with time.[22] Protonated titanate/MoS_2/chromic oxide heterojunction formed by Lu et al. using the solvothermal method showed efficient hydrogen production application.[23] Although these methods have their advantages, they generally involve some kind of local heating which can be challenging to control, and may damage the characteristics of the original building blocks or underlying substructures. Due to these limitations, ion beam welding has become a substitute solution for nanoscale bottom-up joining and assembly, as ion beam welding of nanostructures can be achieved without heating the material and can be focused in small region.[24] In this study, we demonstrate junction formation between hydrogen titanate nanowires (HTNW) and carbon nanotube (CNT) by low energy (50 keV) boron ion beam irradiation. Scanning and transmission electron microscopy confirm the junction formation and TRI3DYN and DFT simulations are employed to understand the joining mechanism and bond formation. One of the direct applications of nano-joining could be electro-mechanical device fabrication through bottom-up approach, where transport characteristic of charge carriers is an important feature. For instance, energy devices require efficient transport of charge carrier to the electrodes or to external circuit. Thus, device with better transport properties would help to gain efficiency.[16] Keeping this prospective in mind, the electrical conductivity has been checked before and after the heterojunction network formation. The low energy ion beam is further known to alter chemical and / or the surface morphology of one-dimensional nano-network. Such changes have been observed to affect the wetting properties of the network. For building a nanodevice, most of the times it is important to have a superhydrophobic surface to protect the device from water condensation and short-circuits. Earlier studies pointed out that irradiation causes titanate nanowires to become hydrophobic and carbon nanotubes to becomes hydrophilic individually.[25–27] In the present study we are dealing with a hybrid form of the two. Therefore, it is interesting to check the fate of this hybrid network after irradiation. Hence this motivated us to study the contact angels of the nano-network before and

after the irradiation. The surface chemical structure is examined by X-ray photoelectron spectroscopy along with the wettability of the surface.

Experimental details

Commercially available multi-walled carbon nanotubes (MWCNT) were purchased from Reinste Nanoventure Pvt. Lt (purity > 95%, number of walls: 3-5, outer diameter: 5-30 nm, inner diameter: 2-6 nm, length: 1-10 μm). Hydrogen titanate ($H_2Ti_3O_7$) nanowires (HTNW) were synthesized hydrothermally. First, anatase TiO_2 powder (99.9% purity) was dissolved in a 10 M NaOH solution and stirred continuously for three days. The solution was then transferred to an autoclave and heated at 180°C for 24 h in a hot-air oven. After heating, the solution was purified multiple times using dilute hydrochloric acid to remove sodium ions. This produces HTNW as the final product, and these were washed with deionized water and dried for final use. HTNW and CNT were mixed in ethanol at 50:50 weight ratio and ultra-sonicated for 1 hour to ensure complete mixing. The resulting mixture was then spin-coated onto pre-cleaned silicon and glass substrates and dried in air.

The coated substrates were subsequently irradiated with 50 keV B^+ ions to fluences of 1×10^{16} and 3×10^{16} ion.cm^{-2} using the ion implantation facilities at the Australian National University. The surface morphology of the samples was analyzed using a Zeiss Ultra Field Emission Scanning Electron Microscope (FESEM). Raman spectra of pristine and irradiated samples were measured using a Jobin Yvon T64000 Micro-Raman spectrometer, facilitated with an inverted microscope. X-ray photoelectron spectroscopy (XPS) analysis was performed at room temperature using a PHI 5000 Versa Probe II, FEI Inc. The contact angle between a deionized water droplet and the sample surface was measured in environmental conditions using a contact angle measurement unit (Apex Instruments Pvt. Ltd, model no. ACAM D1). I–V characteristics were studied using a two-probe method; Two copper probes were connected to the surface of the sample using silver paste. The current was measured by in the voltage range of ± 1 V using a Keithley 6517 electrometer.

Results and discussion

A plan view SEM image of the HTNW and CNT coating is shown in Fig. 1 at different magnifications. The presence of two types of nanostructures is apparent in the image. The thicker and straighter nanostructures are HTNW with an average diameter of 70±10 nm and length in the range of 1-2 μm. The thinner and curly nanostructures are multi-walled CNTs with a length in the range of 1–10 μm and the diameter in the range of 5–30 nm. The nanostructures are well separated from each other, are uniformly mixed, and lay mostly horizontal on the silicon substrate in the pristine sample. As noticeable in Fig. 1 (b) that both the types of nanostructures have smooth surface and sharp edges, and there is no visible interconnections between them in case of as-prepared sample.

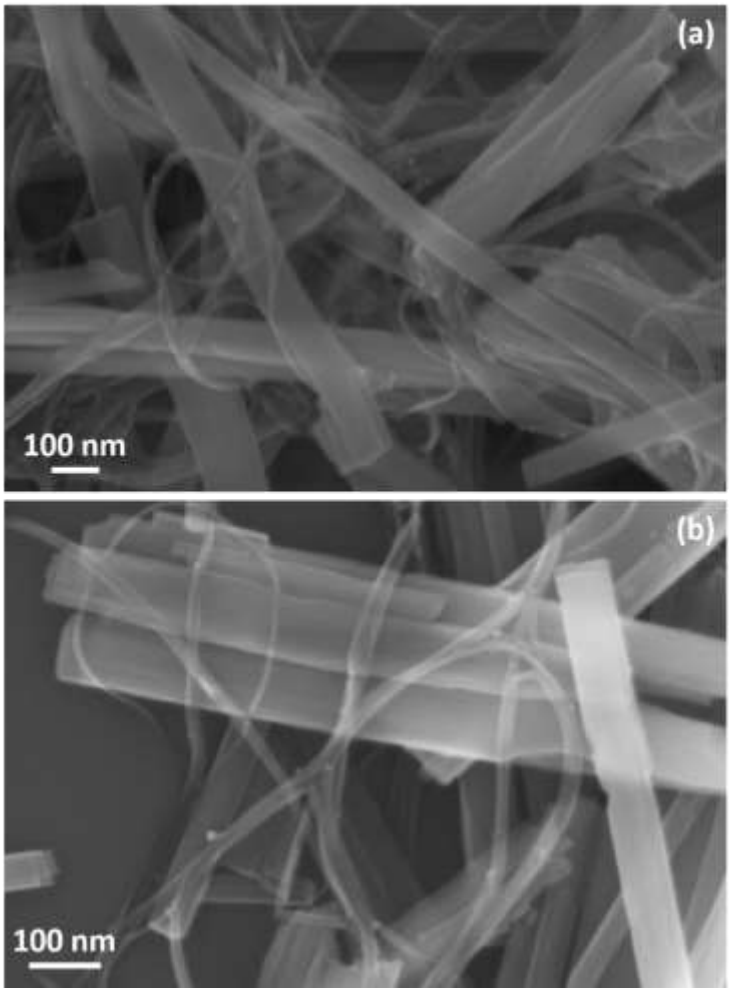

Figure 1: Scanning electron micrographs of the pristine HTNW and CNT film at two different magnifications.

After irradiation with 50 keV B^+ ions to a fluence of 1×10^{16} ions.cm^{-2}, a noticeable change is observed (Fig. 2). At 1×10^{16} ions.cm^{-2} fluence, significant part of the nanostructure is fused and network formation is observed. Fig 2 (b) shows spreading of CNT over HTNW and a clear joining between the two nanostructures. This is further evident from the transmission electron micrograph in Fig. 3 (a), which reveals extensive junction formation between HTNW and CNT. Due to ion induced secondary cascade collision, different atoms from the surface of nanostructures escape and redeposited in between two nanostructure and create a dangling bond. With more atom deposition, these dangling bonds are saturated and create solid junctions.[26] Spreading CNTs is also observed on the Si substrate leading to joining between them (Fig 2 (a)).

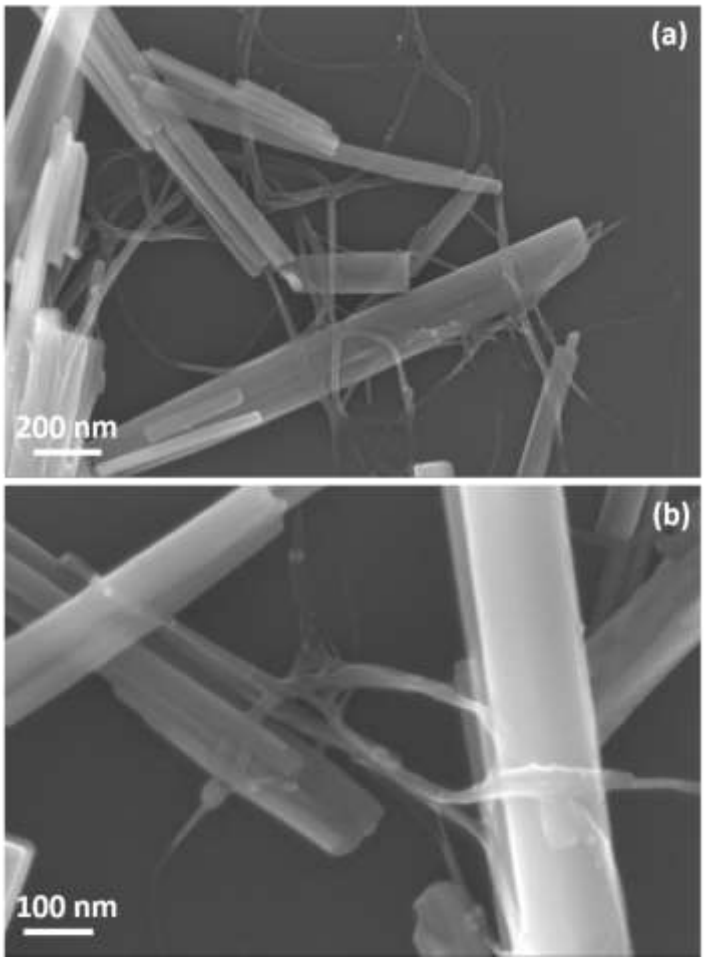

Figure 2: SEM image of the irradiated HTNW and CNT film at 1×10^{16} ions.cm^{-2} fluence at different magnifications.

Selected area electron diffraction (SAED) at the junction areas of the nanostructures after irradiation at 1×10^{16} ions.cm^{-2} fluence is shown in Fig. 3 (b). SAED supports the presence of both the nanostructures in the junction area. In SAED two rings observed at 4.5 and 8.5 mn^{-1} of reciprocal lattice spacing, can be attributed to MWCNT. [28] Along with two rings, several low intense diffraction spots are observed which is assigned to HTNW. HT is formed by edge-shared [TiO_6] octahedral layers in the ABA stacking sequence and bounded by the hydroxyl group. Due to variation in hydroxyl group and low periodicity, HT has very low crystallinity. For this reason, all spots associated with HTNW have relatively low intensity.[16]

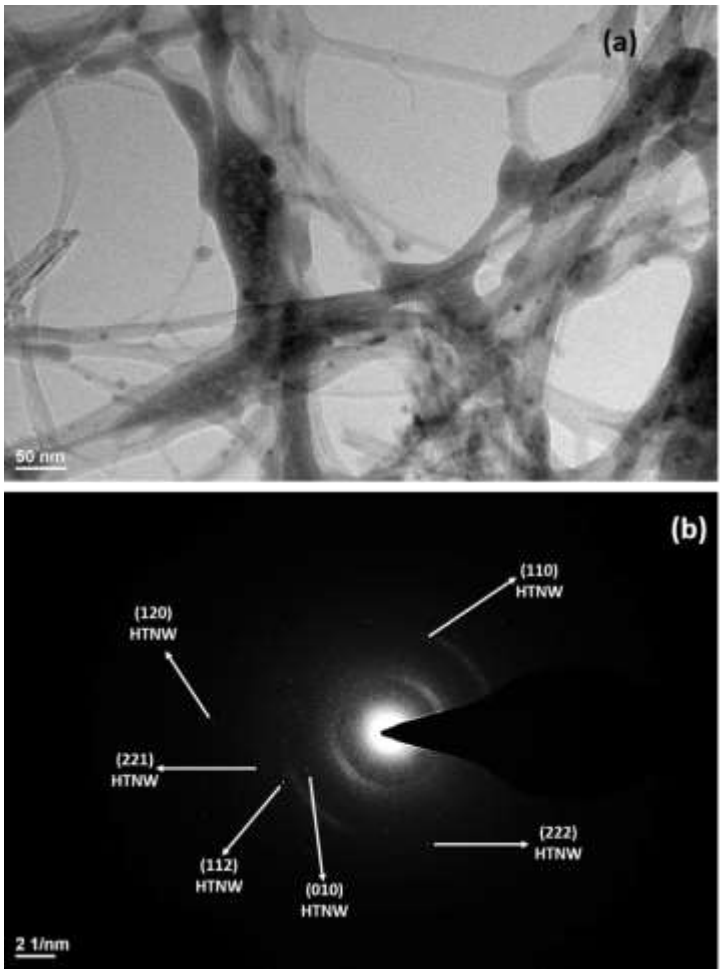

Figure 3: (a) TEM image of the sample irradiated with 1×10^{16} ions.cm^{-2} fluence showing junction formation between HTNW and CNT. (b) SAED image of ion irradiated junction area.

Figure 4 shows scanning electron micrographs of the irradiated HTNW and CNT film at 3×10^{16} ions.cm^{-2} fluence. At a higher fluence, CNT fused into HTNW (Fig. 4 (a)) and loses its structure (Fig. 4 (b)). Nano-protrusions appear on the HTNW surface at higher fluence. Ion collision consequences in different types of sputtering of the nanowire surface. Due to preferential sputtering, light-weight oxygen sputtered out faster than titanium. Sputtering also depends on the slope of the nanowire surface with respect to incident ion beam. Sputtering may increase with increasing slope due to curvature-dependent sputtering. The formation of uneven surface may further enhance the surface-to-volume ratio of the HTNW nanowires.[29,30]

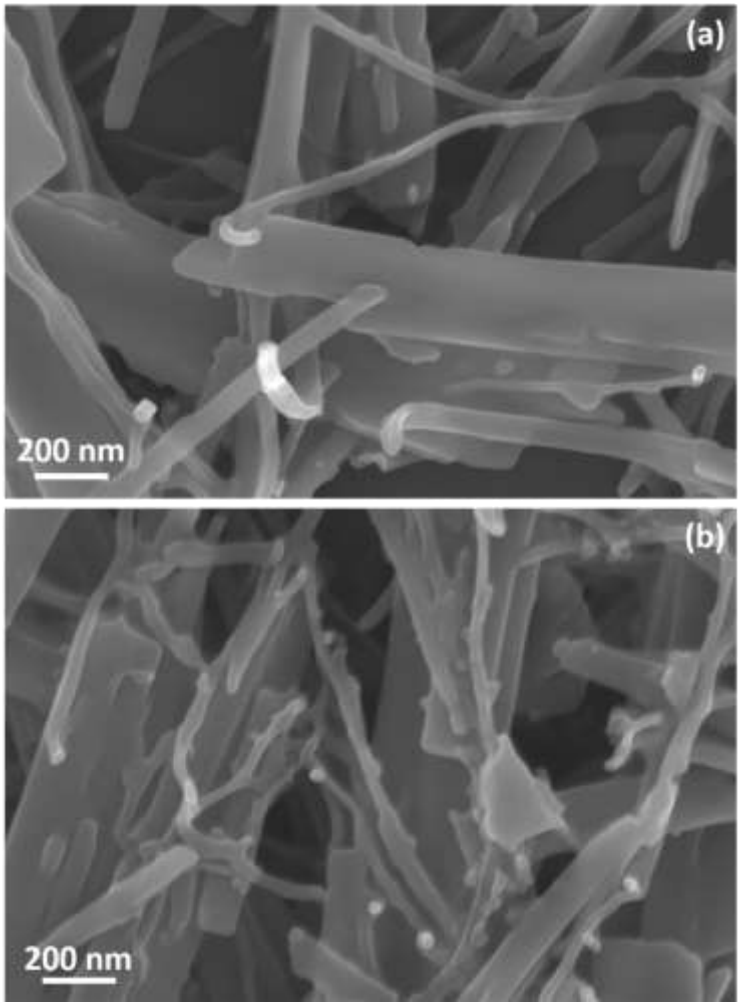

Figure 4: SEM image of the irradiated HTNW and CNT film at 3×10^{16} ions.cm^{-2} fluence.

The energy dispersive spectrum and mapping at the junction area of the HTNW and CNT film irradiated with 3×10^{16} ions.cm^{-2} fluence and the corresponding TEM image is presented in Fig. 5. Energy dispersive spectrum is collected from the yellow-boxed area of the TEM image (Fig 5 (a)), which identifies the presence of titanium K_α peak at around 4.5 keV and K_β transition at around 4.9 keV from (Fig. 5 (b)). Along with titanium, a carbon peak is observed at around 0.3 keV and an oxygen peak at about 0.5 keV. The colored points in the EDS mapping (Fig. 5(c) (e)) also confirm the presence of the elements C, Ti, and O, respectively.

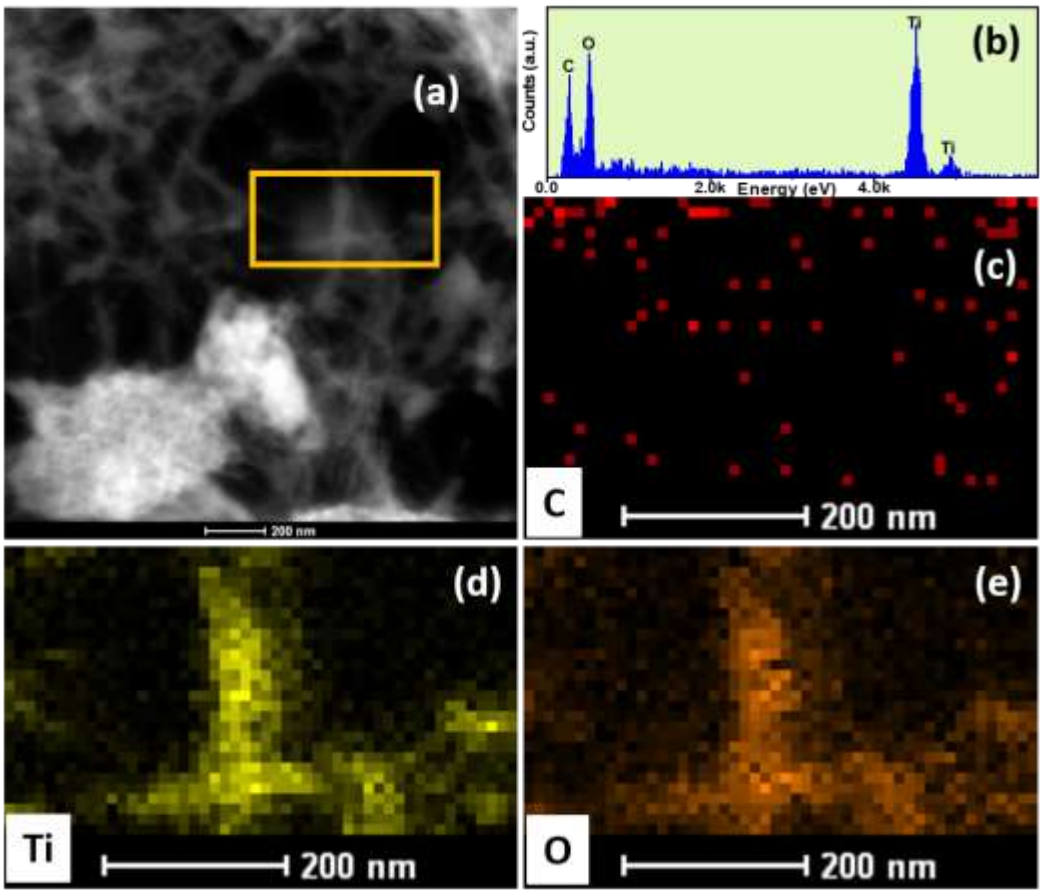

Figure 5: (a) TEM image at junction area of the HTNW and CNT film irradiated with 3×10^{16} ions.cm^{-2} fluence (b) with the EDS spectrum, and corresponding EDS mapping of (c) carbon, (d) titanium, and (e) oxygen.

Irradiation with 50 keV B^+ ions create atomic displacements, leading to recoiled, sputtered target atoms, and bond reorganization. These ballistic effects can be modelled using the TRI3DYN code

which uses Monte Carlo technique to simulate the response of arbitrary 3D structures to ion-irradiation.[31] For the simulation, the HTNW-CNT system was divided into small boxes with dimensions of 150(depth)×250×250 nm^3 (Fig. 6); This volume was divided into 60×100×100 voxels, and in the lateral directions periodic boundary conditions were applied. Two CNTs with 30 nm and 20 nm outer and inner diameters were placed perpendicular to a HTNW of 80 nm diameter. One CNT was placed in contact with one end of the HTNW and the other was placed beneath the HTNW (Fig. 6 (a)). The evolution of this structure was modelled under ion irradiation with 50 keV B^+ ions, with results for fluences of 1×10^{16} ion.cm^{-2} and 3×10^{16} ion.cm^{-2} shown in Fig. 6. For reference, the projected range of 50 keV B^+ ions in HTNW and CNT is 73.6 nm and 62.8 nm, respectively.

The CNT situated at the end of the HTNW is directly impacted by B^+ ions and is more extensively damaged than the underlying CNT. However, even the underlying CNT is damaged at higher fluence due to the increasing contribution from the ions at the end of the range distribution. Even at low fluence, the joining of HTNW and CNT is observed. With increasing fluence, the surface roughness of the nanostructure increases and sputtered atoms from the surfaces redeposit on the junction area increasing the junction thickness (Fig. 6).

Irradiation at the interfaces leads to intermixing, with the movement of the atoms between the nanowires, as shown in Figure 7. Note that these results have been averaged over a central slice of 5 nm thickness. In case of pristine sample, the carbon atomic fractions in the CNT and HTNW are 1.0 and 0.0, respectively. Following irradiation to a fluence of 1×10^{16} ion.cm^{-2}, the carbon atomic fraction in the CNT situated at the edge of the HTNW reduces to 0.8, whereas the carbon atomic fraction in the CNT situated at the bottom of the HTNW remains largely invariant (Fig. 7 (b)). At higher fluence of 3×10^{16} ion.cm^{-2}, the carbon atomic fraction in the CNT placed at the edge of the HTNW decreases to 0.3 and the same in the CNT beneath the HTNW decreases to 0.6 (Fig. 7 (c)). At the same time, the carbon fraction in the HTNW increases, reaching a carbon atomic fraction of nearly 0.25 inside the NW and 0.45 at the bottom edge. O atoms are preferentially sputtered (recoiled) from the bottom of the HTNW, with the average atomic fraction decreasing from 0.7 to 0.3 as the B^+ fluence increases from 1×10^{16} to 3×10^{16} ions.cm^{-2}. Oxygen atoms are also deposited and mixed with the CNT situated at the edge of the HTNW, with atomic fractions of 0.1 and 0.4 estimated for fluences of 1×10^{16} and 3×10^{16} ions.cm^{-2}, respectively. In contrast, the oxygen atomic

fraction in the underlying CNT was 0.00 and 0.13 for fluences of 1×10^{16} and 3×10^{16} ions.cm^{-2} fluence, respectively (Fig. 7 (e, f)).

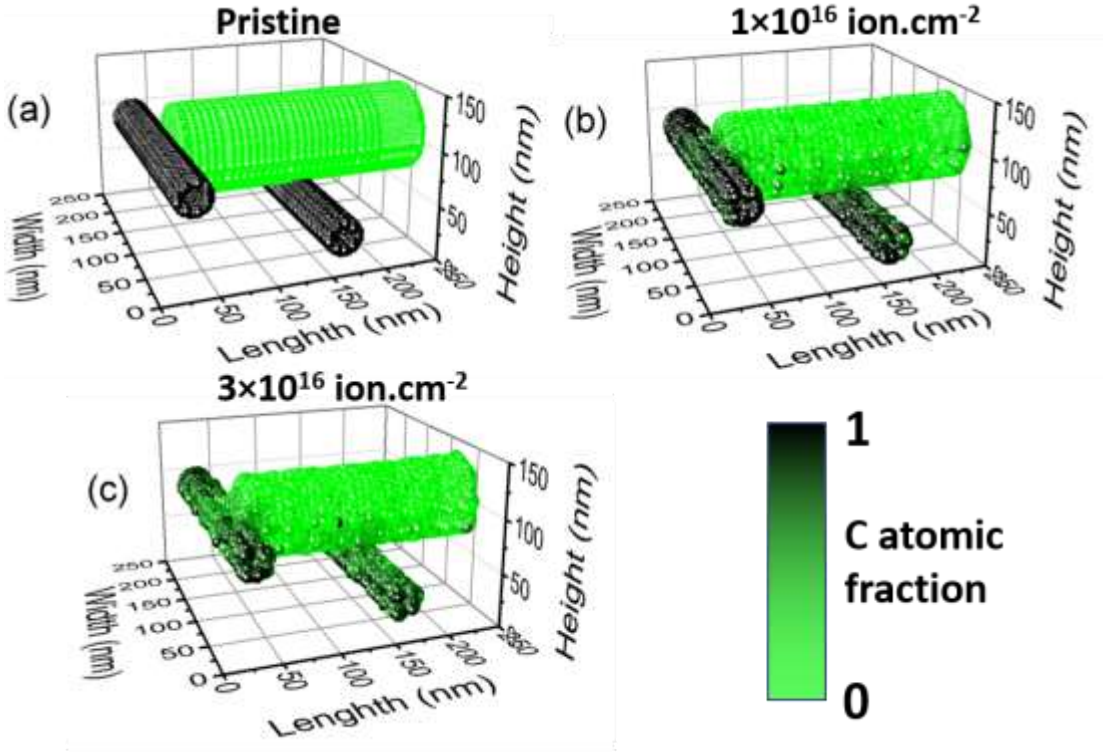

Figure 6: TRI3DYN simulations showing the carbon atomic distribution in two carbon nanotubes with outer diameter of 30 nm and inner diameter of 20 nm, attached to a hydrogen titanate nanowire of diameter 80 nm. Pristine sample (a) and irradiated sample at a fluences of 1×10^{16} ions.cm^{-2} (b) and at a fluence of 3×10^{16} ions.cm^{-2} (c).

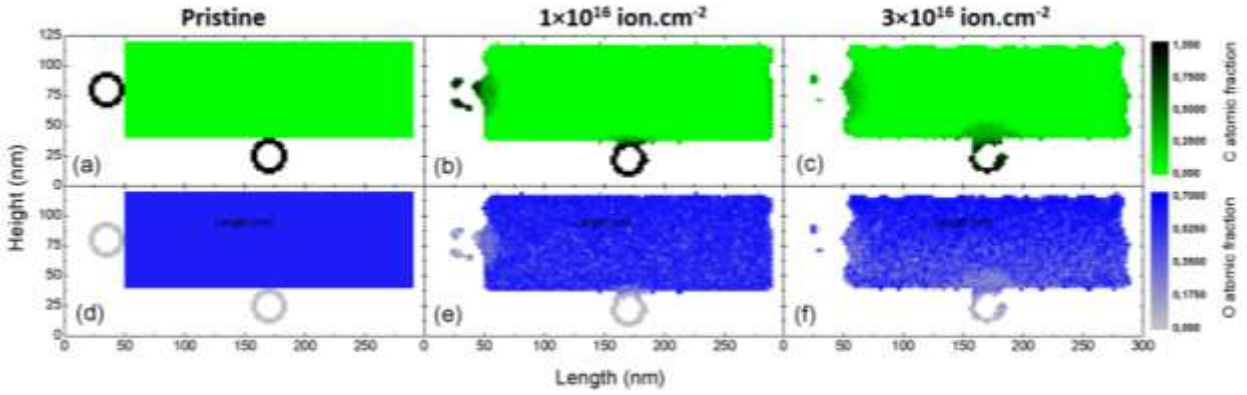

Figure 7: Cross-sectional view of elemental profiles for C (a-c) and O (d-f) for the CNT and HTNW structure. Pristine sample (a,d) and after irradiation to fluences of 1×10^{16} ions.cm^{-2} (b,e) and 3×10^{16} ions.cm^{-2} (c,f).

Figure 8 shows the Raman spectra of pristine and irradiated samples. Four prominent peaks attributed to CNT's are observed for the pristine sample, located at 150, 1345, 1594, and 1746 cm^{-1}.[32] The peak at 1594 cm^{-1}, denoted as G-band (E_{2g}), originates from in-plane vibration of C atoms, which includes the incorporation of bending and stretching of the carbon-carbon (C-C) bonds. The peak at 1345 cm^{-1} corresponds to the disorder-induced D-band (A_{1g}), a highly dispersive spectral feature, which is due to the combined in-plane vibration of atoms towards and away from the center of the covalently (sp^2) bonded hexagons carbon atoms. The ratio of D and G peaks is known as the disorder parameter.[33] The disorder parameter represents the degree of defects in CNT. After the baseline corrections, the disorder parameters of all samples have been calculated using the ratio of peak area. For the pristine sample, the value of the disorder parameter is 0.015, which increases with increasing ion fluence and becomes 0.047 and 2.281 at fluences of 1×10^{16} and 3×10^{16} ions·cm^{-2}, respectively. After irradiation, the disorder parameter increases drastically, indicate the disordering and amorphization of the CNTs.[34] The peak situated at 150 cm^{-1} associated with radial breathing mode (RBM). The RBM mode is correlated to vibrational movement of the all carbon atoms towards and away from the central axis of CNT.[35] The peak at 1746 cm^{-1}, denoted as M-band, originates due to second-order overtone of out-plane tangential optical phonon mode contribute to those electron-phonon modes for (q=0). M band associated with diameter-dependent curvature of CNT.[36] With increasing ion fluence, CNT loses its structure and the relative intensity of both RBM mode and M band decreases. Several small peaks observed at 175, 1086, and 1136 cm^{-1} in the pristine sample originate from the HTNW and are due to Ti-O, Ti-O-H, and Ti-O-Ti bond vibration.[37][38] The intensity of these peaks decreases following irradiation.

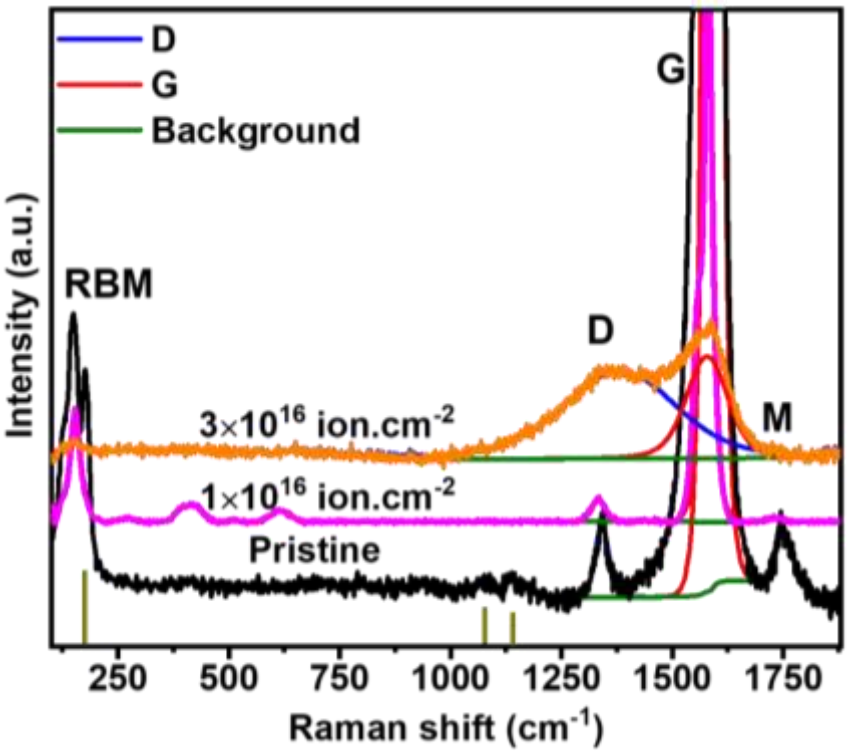

Figure 8: Raman spectra of pristine and irradiated samples at ion fluences of 1×10^{16} and 3×10^{16} ion.cm^{-2}.

Ti 2p core-level X-ray photoelectron spectra of pristine and irradiated (3×10^{16} ions.cm^{-2}) samples are shown in Fig. 9 (a) and (d), along with the components after spectral decomposition. The two peaks situated at 458.7 and 464.5 eV are assigned to the Ti $2p_{3/2}$ and $2p_{1/2}$ levels of the Ti 4^+ valence state.[39] No noticeable change is observed in the Ti 2p XPS peaks after irradiation, suggesting that the Ti 4^+ valence state responsible for O-Ti-O bond formation in both HTNW and TiO_2 remains dominant. Figure 9 (b) and (e) shows detailed C 1*s* core-level XPS spectra acquired from the pristine and the irradiated sample, with peaks situated at 283.9 and 284.7 eV assigned to carbon sp^2 and sp^3 hybridization, respectively. The binding energies for C-O-C and C-OH bonding are assigned at 289.9 and 288.4 eV, respectively.[34] The peak areas of the sp^2 and C-O-C peaks are significantly affected by irradiation, with the relative intensity of the C=C bond (sp^2) decreasing due to structural deformation of the CNT, a feature evident in the TRI3DYN simulations. The relative intensity of the C-O-C's increases post-irradiation, which may be attributed to bond formation between carbon and the HTNW or environmental oxygen. A significant chemical shift

is also observed in the O 1s spectra, with Fig. 9 (c) and (f) showing detailed O 1*s* core level XPS spectra acquired from the pristine and the irradiated sample. Three peaks are observed in the O 1s spectra; the peak at 530.1 eV arises from the Ti-O bond present in HTNW, while at 531.8 eV is due to both the O-H bond in HTNW and water present in the sample, and the peak at 530.7 eV is assigned to the C-O bond.[40] In case of pristine sample the area ratios for the Ti-O, C-O, and H-O peaks was 4:1:5, while after irradiation they were 10:5:4. At 90% confidence interval, the variation in the area ratios of the Ti-O, C-O, and H-O peaks for the pristine and irradiated sample were ±0.414 and ±0.446, respectively. In the irradiated samples the relative peak area of Ti-O increases due to ion induced bond reorganization. Due to the preferential sputtering of oxygen from the surface hydroxyl group less H-O is present in the irradiated sample and the relative fraction of C-O increases by more than factor of two.

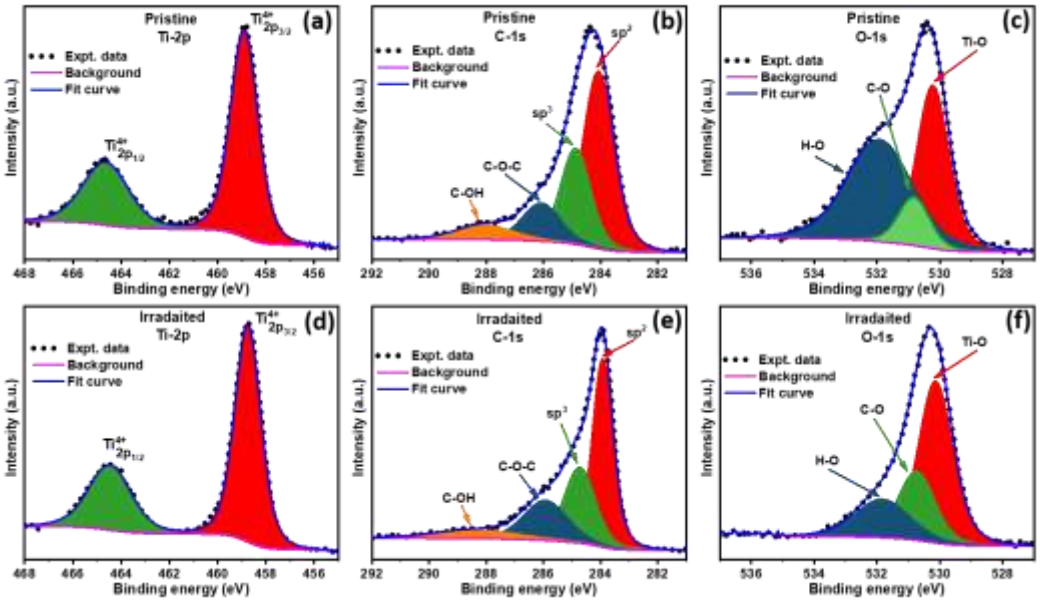

Figure 9: XPS spectra of Ti-2p, C-1s, and O-1s for pristine (a, b, and c) and irradiated at 3×10^{16} ion.cm^{-2} (d, e, and f) for HTNW and CNT ensemble.

To better understand the dominant bonding mechanisms, pristine and irradiated HTNW and CNT assemblies were studied using DFT simulations. To represent the pristine structure, we placed a slice of CNT on a slice of HTNW at 0.2 nm distance from the top surface, and allowed the structure

to relax. To understand the irradiation effect, five different structures were then created by introducing O and C vacancy and non-lattice O and C atoms in relaxed pristine structure. The DFT calculation of total energies was performed using Rappe-Rabe-Kaxiras-Joannopoulos ultrasoft (RRKJUS) pseudopotentials within the Perdew-Burke-Ernzerhof (PBE) approximation of exchange-correlation functional. The plane wave cutoff energy was set at 25 Ry and the density cutoff at 225 Ry, the convergence threshold for self-consistency was set at 10^{-6} Ry. The lattice parameters and all atoms' positions were relaxed until the force was less than 1×10^{-3} Ry/Bohr. All calculations were performed using the Quantum ESPRESSO (QE, version 6.2).[41] Mechanical strength of all bond calculated using the model described by Guo et al.[42]

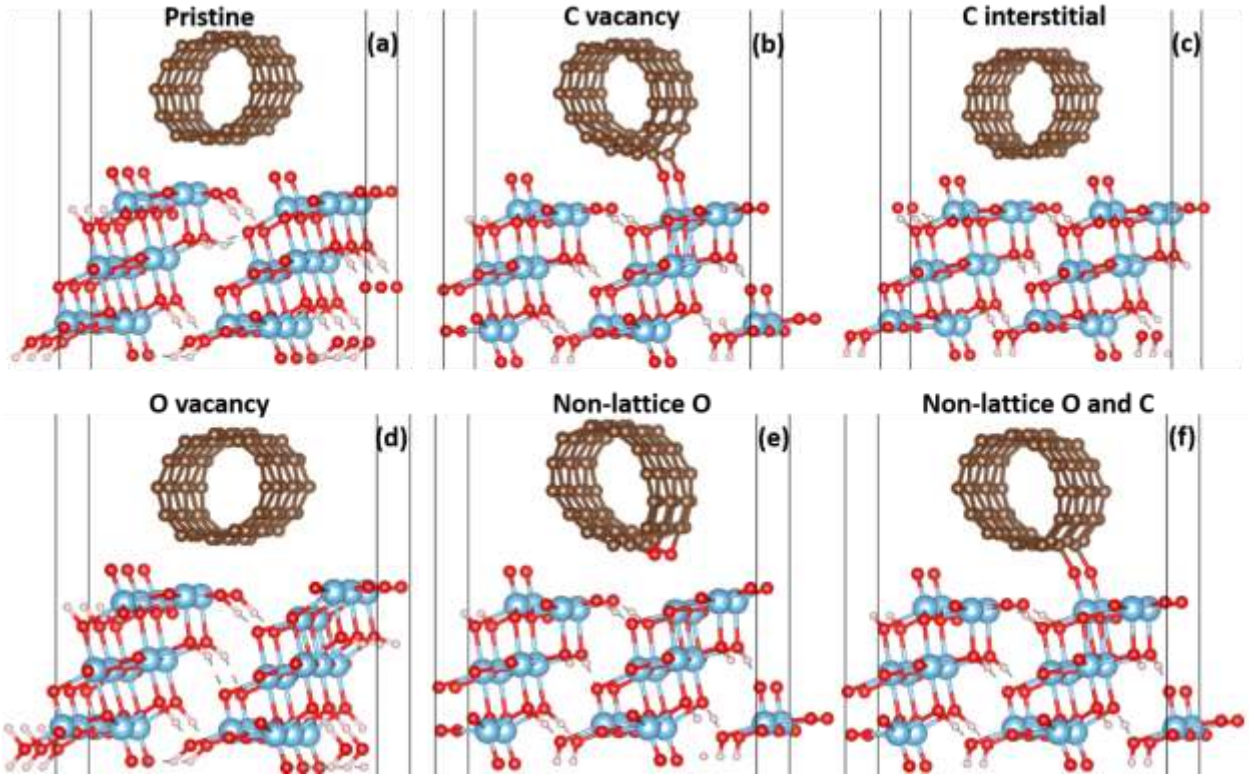

Figure 10: Optimized geometries of pristine (a) and irradiated HTNW and CNT ensembles with O and C vacancy and non-lattice O and C (b, c, d, e, and f).

Optimized pristine HTNW and CNT assemblies are shown in Fig. 10 (a). After optimization, the CNT moves away from the HTNW, indicating no possible bond formation between unmodified HTNW and CNT. Figure 10 (b) shows an optimized mixed structure with a C vacancy, showing

C-O-Ti bond formation between the HTNW and CNT and the mechanical strength of the bond is 6.4 nN. Figure 10 (c) shows an optimized mixed structure with a non-lattice C, placed between CNT and HTNW. During optimization, the interstitial C atom moves back to the CNT, and no bond is formed. Figure 10 (d) shows an optimized mixed structure with an O vacancy. The optimized structure shows no bond formation or attraction between HTNW and CNT. Figure 10 (e) shows optimized HTNW and CNT ensembles with an O atom placed between CNT and HTNW. The optimized structure shows C-O-C bond formation in the CNT but no bond is formed between the two nanostructures, which is evident from XPS spectra. Figure 10 (f) shows an optimized mixed structure with non-lattice C and O atoms, placed between CNT and HTNW. In the optimized structure, C atoms move to the CNT and O moves to the HTNW structure, and a C-O-Ti bond is formed between the HTNW and CNT and the mechanical strength of the bond is 5.55 nN. In all possible irradiated structures, bonds formed only when C vacancies are present and both O and C atoms simultaneously present in between HTNW and CNT.

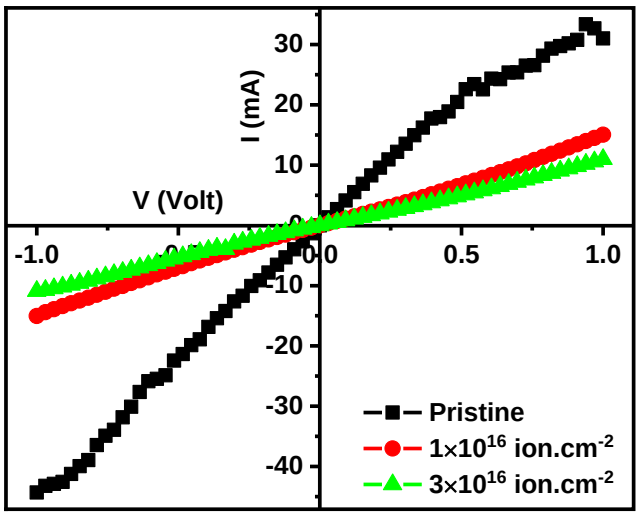

Figure 11: I–V curves for a pristine HTNW and CNT ensembles (black) and for ensembles irradiated with 50 keV B^+ ions at fluences of 1×10^{16} (red) and 3×10^{16} ions·cm^{-2} (green).

I-V measurements of pristine and irradiated HTNW and CNT ensembles were measured with a Keithley 6517B electrometer using the two-probe method; Two copper probes placed 10 mm apart, connected using silver paste. The pristine HTNW and CNT ensembles displayed a near Ohmic characteristic with currents of -44.32 and 31.02 mA measured at voltages of -1 and +1 V (Fig. 11).

The resistance increased with the increasing ion fluence, such that the sample irradiated to a fluence of 1×10^{16} ions.cm^{-2} recorded currents of -15.04 to 15.04 mA, the sample irradiated to a fluence of 3×10^{16} ions.cm^{-2} recorded currents of -10.90 to 10.99 mA for -1 V and +1V, respectively. Such analysis shows that the pristine sample has a conductivity of 2.2×10^{5} S.m^{-1} due to the presence of highly conductive unmodified CNT, while that of the irradiated samples is 6.0×10^{4} S.m^{-1} after irradiation to a fluence of 1×10^{16} ions.cm^{-2}and $4.7\text{x}10^{4}$ S.m^{-1} after a fluence of 3×10^{16} ions.cm^{-2}. Despite this reduction, the conductivity of the irradiated HTNW and CNT mixture is about three times higher than irradiated hydrogen titanate.[26] This opens up the possibility of fabrication of more efficient hydrogen titanate based nanodevice.

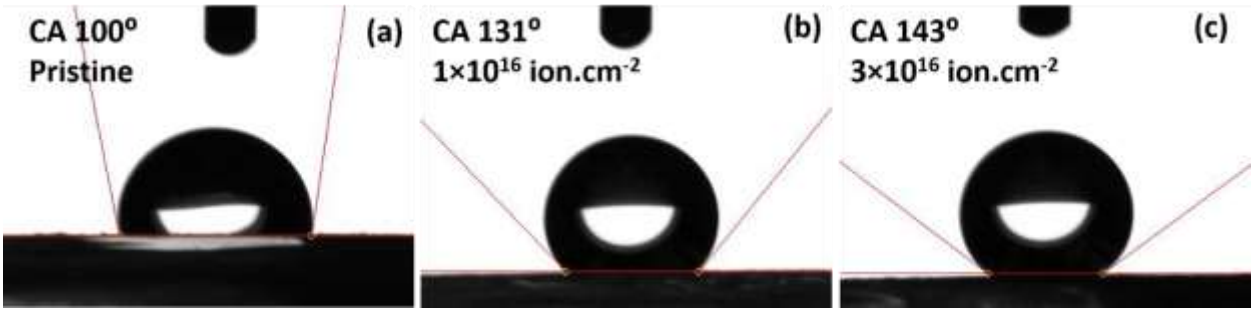

Figure 12: Contact angle of a water droplet on (a) a pristine and on HTNW and CNT ensembles and on films irradiate with 50 keV B^{+} to fluences of (b) 1×10^{16} and (c) 3×10^{16} ions·cm^{-2}.

Interaction of water with pristine and irradiated HTNW and CNT ensembles was examined using static and dynamic contact angle measurements of a water droplet. The water droplet on the pristine surface makes a contact angle of 100º±2.8º (Fig. 12 (a)). With increasing ion fluence, the contact angle increases. After irradiation with 1×10^{16} ions.cm^{-2} the contact angle increases to 131º±1.55º (Fig. 12 (b)) and after irradiation with 3×10^{16} ions.cm^{-2} it increases further to 143º±0.8º (Fig. 12 (c)). Both the pristine and the irradiated surfaces are hydrophobic. The evolution of water droplets on the sample surface was been observed for 10 minutes, and characterized by the height of the drop (h), the contact radius (r_b), the radius of the sphere (R_S), and the contact angle (θ) characteristic parameters. The diffusion coefficient (D) was calculated using Fick's law of diffusion for water droplets using these parameters.[43,44] In the case of the pristine sample, contact angle, and contact height change significantly but the contact radius remains almost constant (Fig. S1); the contact angle changes from 100º to 32º within 10 minutes (Fig. S1 (a)),

giving a diffusion coefficient of 6.30×10^{-5} $m^{-2}sec^{-1}$, which is very high compared with the normal evaporation of water droplets at room temperature. In case of the sample irradiated with 3×10^{16} ions.cm^{-2} the contact angle, contact height, and contact radius remain almost constant. The contact angle changes from 143º to 139º over the same duration. In this case the diffusion coefficient is estimated to be 2.14×10^{-5} $m^{-2}sec^{-1}$, comparable to the normal evaporation of water droplets into the environment at room temperature.[45] Changes in the wetting behavior of the pristine sample result from competitions between different wetting properties of the constituent materials. The pristine surface is hydrophobic due to the presence of superhydrophobic CNT but hydrogen titanate contains a high concentration of -OH groups which attracts water molecules, leading to fast absorption of water. The change in contact radius and the estimated diffusion coefficient indicate droplet did not spread over the sample surface or evaporate in this case. Ion irradiation removes -OH groups from the surface and creates 3D porous network structure through ion-induced joining of the nanowires. Air trapped in the porous network repels water from the surface and it behaves as a Cassie-Baxter like surface.[29,43] Due to reduction of -OH groups and the Cassie-Baxter like behavior, the irradiated surface is hydrophobic in nature.

Conclusions

In conclusion, we have demonstrated heterojunction formation between carbon nanotubes and metal oxide nanowire by energetic ion-irradiation. Irradiation with 50 keV B^+ ions to fluences in the range from 1×10^{16} to 3×10^{16} ions.cm^{-2} were shown to produce a well interconnected 3D nano-network of nanowires and nanotubes. Details of the ion beam modification and associated bonding processes have been corroborated by 3D Monte Carlo based TRI3DYN simulation code and the DFT calculations, respectively. The TRI3DYN simulations detailed the redistribution and ion beam mixing resulting from ballistic collisions between the incident ion and target atoms. With increasing fluence, the surface roughness of the nanostructure increased and sputtered and recoiled atoms were redeposited at the nanostructure junctions and subsequently intermixed to form welded junctions. The 3D network structure and surface roughness produced a highly porous structure with large surface area as well as volume. Raman scattering confirmed gradual amorphization of the nanostructures, while XPS analysis and DFT simulations showed that bond formation between the HTNW and CNT was mediated by a combination of carbon vacancies and non-lattice oxygen

and carbon atoms produced during irradiation. The electrical conductivity of the irradiated nanostructures was found to be about three times higher than that of irradiated hydrogen titanate, opening up the possibility of fabrication more efficient hydrogen titanate based nanodevice. Water contact-angle measurements showed that the pristine HTNW and CNT ensemble was hydrophobic and that it became more hydrophobic with increasing ion irradiation. This water repelling property provides an advantage for this structure to avoid water condensation as well as to avoid water-borne corrosions.

Acknowledgments

We would like to acknowledge access to the Australian Facility for Advanced ion-implantation Research (AFAiiR), an NCRIS funded research facility located the Australian National University, for the ion-irradiations. SC acknowledges the financial supports from the Department of Science and Technology (Technology Mission Division), India for project grant no. DST/TMD-EWO/WTI/2K19/EWFH/2019/164 and SERB (DST) for grant no. EMR/2017/000509 and FESEM, XRD facilities of IIT Bhubaneswar.

References

[1] Z.L. Petrovi, P. Maguire, M. Radmilovi, N. Puaˇ, D. Mari, C. Mahony, G. Malovi, Nanotechnology for Electronics, Photonics, and Renewable Energy, (2010) 211–243. https://doi.org/10.1007/978-1-4419-7454-9.

[2] M. Moreno-Moreno, P. Ares, C. Moreno, F. Zamora, C. Gómez-Navarro, J. Gómez-Herrero, AFM Manipulation of Gold Nanowires to Build Electrical Circuits, Nano Lett. 19 (2019) 5459–5468. https://doi.org/10.1021/acs.nanolett.9b01972.

[3] B. Seong, I. Chae, H. Lee, V.D. Nguyen, D. Byun, Spontaneous self-welding of silver nanowire networks, Phys. Chem. Chem. Phys. 17 (2015) 7629–7633. https://doi.org/10.1039/c5cp00035a.

[4] H. Kang, Y. Kim, S. Cheon, G.R. Yi, J.H. Cho, Halide Welding for Silver Nanowire Network Electrode, ACS Appl. Mater. Interfaces. 9 (2017) 30779–30785. https://doi.org/10.1021/acsami.7b09839.

[5] P. Peng, W. Guo, Y. Zhu, L. Liu, G. Zou, Y.N. Zhou, Nanoscale wire bonding of individual ag nanowires on au substrate at room temperature, Nano-Micro Lett. 9 (2017) 1–6. https://doi.org/10.1007/s40820-017-0126-8.

[6] M.D. Ho, Y. Ling, L.W. Yap, Y. Wang, D. Dong, Y. Zhao, W. Cheng, Percolating Network of Ultrathin Gold Nanowires and Silver Nanowires toward “Invisible” Wearable Sensors for Detecting Emotional Expression and Apexcardiogram, Adv. Funct. Mater. 27 (2017) 1700845. https://doi.org/10.1002/adfm.201700845.

[7] J. Wang, F. Gao, Z. Gu, Infrared (IR) Soldering of Metallic Nanowires, in: Proc. - Electron. Components Technol. Conf., Institute of Electrical and Electronics Engineers Inc., 2017: pp. 2175–2180. https://doi.org/10.1109/ECTC.2017.181.

[8] M.J. Crane, E.P. Pandres, E.J. Davis, V.C. Holmberg, P.J. Pauzauskie, Optically oriented attachment of nanoscale metal-semiconductor heterostructures in organic solvents via photonic nanosoldering, Nat. Commun. 10 (2019) 1–7. https://doi.org/10.1038/s41467-019-12827-w.

[9] Y. Qin, J. Zang, Stable clusters array of silicon nanowires developed by top-plating technique as a high-performance gas sensor, Phys. E Low-Dimensional Syst. Nanostructures. 127 (2021) 114508. https://doi.org/10.1016/j.physe.2020.114508.

[10] F. Shao, J.D. Fan, F. Hernández-Ramírez, C. Fàbrega, T. Andreu, A. Cabot, J.D. Prades, N. López, F. Udrea, A. De Luca, S.Z. Ali, J.R. Morante, NH3 sensing with self-assembled ZnO-nanowire $μ$hP sensors in isothermal and temperature-pulsed mode, Sensors Actuators, B Chem. 226 (2016) 110–117. https://doi.org/10.1016/j.snb.2015.11.109.

[11] G. Liu, Q. Li, M. Qiu, Sacrificial solder based nanowelding of ZnO nanowires, in: J. Phys. Conf. Ser., Institute of Physics Publishing, 2016: p. 012027. https://doi.org/10.1088/1742-6596/680/1/012027.

[12] F. Hernández-Ramírez, J. Rodríguez, O. Casals, E. Russinyol, A. Vilà, A. Romano-

Rodríguez, J.R. Morante, M. Abid, Characterization of metal-oxide nanosensors fabricated with focused ion beam (FIB), Sensors Actuators, B Chem. 118 (2006) 198–203. https://doi.org/10.1016/j.snb.2006.04.022.

[13] L. Zhang, X. Zhang, G. Tian, Q. Zhang, M. Knapp, H. Ehrenberg, G. Chen, Z. Shen, G. Yang, L. Gu, F. Du, Lithium lanthanum titanate perovskite as an anode for lithium ion batteries, Nat. Commun. 11 (2020) 1–8. https://doi.org/10.1038/s41467-020-17233-1.

[14] A. Somdee, Improved photovoltaic efficiency of dye sensitized solar cells by decorating TiO2 photoanode with barium titanate oxide, J. Alloys Compd. 777 (2019) 1251–1257. https://doi.org/10.1016/j.jallcom.2018.11.085.

[15] G.A.M. Mersal, N.Y. Mostafa, A.E.H. Omar, Hydrothermal synthesis and processing of hydrogen titanate nanotubes for nicotine electrochemical sensing, Mater. Res. Express. 4 (2017) 085031. https://doi.org/10.1088/2053-1591/aa83de.

[16] P. Das, S. Das, S. Ratha, B. Chakraborty, S. Chatterjee, Ion beam engineered hydrogen titanate nanotubes for superior energy storage application, Electrochim. Acta. 371 (2021) 137774. https://doi.org/10.1016/j.electacta.2021.137774.

[17] Y. Yao, F. Jiang, C. Yang, K.K. Fu, J. Hayden, C.F. Lin, H. Xie, M. Jiao, C. Yang, Y. Wang, S. He, F. Xu, E. Hitz, T. Gao, J. Dai, W. Luo, G. Rubloff, C. Wang, L. Hu, Epitaxial Welding of Carbon Nanotube Networks for Aqueous Battery Current Collectors, ACS Nano. 12 (2018) 5266–5273. https://doi.org/10.1021/acsnano.7b08584.

[18] K. Matsumoto, T. Ishikawa, T. Tanaka, A novel joining method by using carbon nanotube-based thermoplastic film for injection over-molding process, J. Reinf. Plast. Compos. 38 (2019) 616–627. https://doi.org/10.1177/0731684419838070.

[19] S. Jiang, P.X. Hou, M.L. Chen, B.W. Wang, D.M. Sun, D.M. Tang, Q. Jin, Q.X. Guo, D.D. Zhang, J.H. Du, K.P. Tai, J. Tan, E.I. Kauppinen, C. Liu, H.M. Cheng, Ultrahigh-performance transparent conductive films of carbon-welded isolated single-wall carbon nanotubes, Sci. Adv. 4 (2018) eaap9264. https://doi.org/10.1126/sciadv.aap9264.

[20] H. Tanaka, M. Akai-Kasaya, A. Termehyousefi, L. Hong, L. Fu, H. Tamukoh, D. Tanaka, T. Asai, T. Ogawa, A molecular neuromorphic network device consisting of single-walled

carbon nanotubes complexed with polyoxometalate, Nat. Commun. 9 (2018) 1–7. https://doi.org/10.1038/s41467-018-04886-2.

[21] N.X. Sang, V.C. Minh, Thermal annealing-induced self-junction of hydrothermal titanate nanotubes/TiO2nanoparticles with enhanced photocatalytic activity, Nanotechnology. 31 (2020) 435703–435710. https://doi.org/10.1088/1361-6528/aba65c.

[22] S. Hirose, S. Ueda, N. Ohashi, Effect of aging on the current transport properties at gold/niobium-doped strontium titanate Schottky junctions, J. Appl. Phys. 125 (2019) 095301. https://doi.org/10.1063/1.5066574.

[23] D. Lu, Q. Wang, K.K. Kondamareddy, A. Wang, H. Hao, Q. Wu, Efficiently visible-light-induced photoactivity of MoS2 nanoflowers/chromic oxide/protonated titanate nanoflakes edge-on ternary heterostructures for production of hydrogen, J. Alloys Compd. 761 (2018) 31–40. https://doi.org/10.1016/j.jallcom.2018.05.149.

[24] M.K. Rajbhar, P. Das, B. Satpati, W. Möller, S. Facsko, R. Böttger, N. Ramgir, S. Chatterjee, Joining of two different ceramic nanomaterials for bottom-up fabrication of heterojunction devices, Appl. Surf. Sci. 478 (2019) 651–660. https://doi.org/10.1016/j.apsusc.2019.02.002.

[25] P. Das, S. Dhal, S. Ghosh, S. Chatterjee, C.S. Rout, N. Ramgir, S. Chatterjee, Superhydrophobic to hydrophilic transition of multi-walled carbon nanotubes induced by Na + ion irradiation, Nucl. Instruments Methods Phys. Res. Sect. B Beam Interact. with Mater. Atoms. 413 (2017) 31–36. https://doi.org/10.1016/j.nimb.2017.10.004.

[26] S. Dhal, P. Das, M.K. Rajbhar, W. Möller, S. Chatterjee, N. Ramgir, S. Chatterjee, Superior electrical conduction of a water repelling 3D interconnected nano-network, J. Mater. Chem. C. 6 (2018) 1951–1958. https://doi.org/10.1039/C7TC05374F.

[27] P. Das, S. Chatterjee, Tuning wettability of hydrogen titanate nanowire mesh by Na+irradiation, in: AIP Conf. Proc., AIP Publishing LLC, 2018: p. 80017. https://doi.org/10.1063/1.5028851.

[28] I.A. Mohammed, M.T. Bankole, A.S. Abdulkareem, S.S. Ochigbo, A.S. Afolabi, O.K. Abubakre, Full factorial design approach to carbon nanotubes synthesis by CVD method

in argon environment, South African J. Chem. Eng. 24 (2017) 17–42. https://doi.org/10.1016/j.sajce.2017.06.001.

[29] P. Das, M.K. Rajbhar, R.G. Elliman, W. Möller, S. Facsko, S. Chatterjee, Nanoscale modification of one-dimensional single-crystalline cuprous oxide, Nanotechnology. 30 (2019) 365304. https://doi.org/10.1088/1361-6528/ab2018.

[30] M.K. Rajbhar, W. Möller, B. Satpati, U. Manju, Y.S. Chaudhary, S. Chatterjee, W. Moeller, B. Satpati, U. Manju, Y.S. Chaudhary, S. Chatterjee, Broad Beam-Induced Fragmentation and Joining of Tungsten Oxide Nanorods: Implications for Nanodevice Fabrication and the Development of Fusion Reactors, ACS Appl. Nano Mater. 3 (2020) 9064–9075. https://doi.org/10.1021/acsanm.0c01750.

[31] W. Möller, TRI3DYN – Collisional computer simulation of the dynamic evolution of 3-dimensional nanostructures under ion irradiation, Nucl. Instruments Methods Phys. Res. Sect. B Beam Interact. with Mater. Atoms. 322 (2014) 23–33. https://doi.org/10.1016/J.NIMB.2013.12.027.

[32] W. Cui, T. Saito, P. Ayala, T. Pichler, L. Shi, Oxidation stability of confined linear carbon chains, carbon nanotubes, and graphene nanoribbons as 1D nanocarbons, Nanoscale. 11 (2019) 15253–15258. https://doi.org/10.1039/c9nr04924j.

[33] C. Tyagi, S.A. Khan, S. Ojha, D.K. Avasthi, A. Tripathi, Effect of carbon ion-beam irradiation on graphene oxide film, Vacuum. 154 (2018) 259–263. https://doi.org/10.1016/j.vacuum.2018.05.003.

[34] P. Das, B. Rout, U. Manju, S. Chatterjee, Tunable Wettability and Conductivity of the Graphene Oxide Surface with Insights from Density Functional Theory and Molecular Dynamics Investigations, J. Phys. Chem. C. 124 (2020) 10541–10549. https://doi.org/10.1021/acs.jpcc.0c01166.

[35] X.W. Lei, Q.Q. Ni, J.X. Shi, T. Natsuki, Radial breathing mode of carbon nanotubes subjected to axial pressure, Nanoscale Res. Lett. 6 (2011) 1–6. https://doi.org/10.1186/1556-276X-6-492.

[36] K. Yokoyama, Y. Sato, M. Yamamoto, T. Nishida, T. Itoh, K. Motomiya,

Functionalization of primary amine groups to single-walled carbon nanotubes by reacting fluorinated SWCNTs with ammonia gas at a low temperature, Carbon N. Y. 172 (2021) 360–371. https://doi.org/10.1016/j.carbon.2020.10.038.

[37] H. Park, T. Goto, D.H. Han, S. Cho, H. Nishida, T. Sekino, Low Alkali Bottom-Up Synthesis of Titanate Nanotubes Using a Peroxo Titanium Complex Ion Precursor for Photocatalysis, ACS Appl. Nano Mater. 3 (2020) 7795–7803. https://doi.org/10.1021/acsanm.0c01347.

[38] Y. Kanazawa, A. Itadani, H. Hashimoto, K. Uematsu, K. Toda, M. Sato, Room temperature adsorption of propene and propane on copper ions distributed in titanate nanotubes, Appl. Surf. Sci. 483 (2019) 642–651. https://doi.org/10.1016/j.apsusc.2019.03.328.

[39] X. Lu, G. Wang, T. Zhai, M. Yu, J. Gan, Y. Tong, Y. Li, Hydrogenated TiO 2 nanotube arrays for supercapacitors, Nano Lett. 12 (2012) 1690–1696. https://doi.org/10.1021/nl300173j.

[40] W. Li, J. Wang, G. He, L. Yu, N. Noor, Y. Sun, X. Zhou, J. Hu, I.P. Parkin, Enhanced adsorption capacity of ultralong hydrogen titanate nanobelts for antibiotics, J. Mater. Chem. A. 5 (2017) 4352–4358. https://doi.org/10.1039/c6ta09116d.

[41] P. Giannozzi, S. Baroni, N. Bonini, M. Calandra, R. Car, C. Cavazzoni, D. Ceresoli, G.L. Chiarotti, M. Cococcioni, I. Dabo, A. Dal Corso, S. de Gironcoli, S. Fabris, G. Fratesi, R. Gebauer, U. Gerstmann, C. Gougoussis, A. Kokalj, M. Lazzeri, L. Martin-Samos, N. Marzari, F. Mauri, R. Mazzarello, S. Paolini, A. Pasquarello, L. Paulatto, C. Sbraccia, S. Scandolo, G. Sclauzero, A.P. Seitsonen, A. Smogunov, P. Umari, R.M. Wentzcovitch, QUANTUM ESPRESSO: a modular and open-source software project for quantum simulations of materials, J. Phys. Condens. Matter. 21 (2009) 395502. https://doi.org/10.1088/0953-8984/21/39/395502.

[42] X. Guo, L.M. Wang, B. Xu, Z. Liu, D. Yu, J. He, H.T. Wang, Y. Tian, Unbinding force of chemical bonds and tensile strength in strong crystals, J. Phys. Condens. Matter. 21 (2009) 485405. https://doi.org/10.1088/0953-8984/21/48/485405.

[43] T.S. Wong, S.H. Kang, S.K.Y. Tang, E.J. Smythe, B.D. Hatton, A. Grinthal, J. Aizenberg, Bioinspired self-repairing slippery surfaces with pressure-stable omniphobicity, Nature. 477 (2011) 443–447. https://doi.org/10.1038/nature10447.

[44] A.K. Behera, P. Das, I. Thakur, S. Chatterjee, S. Chatterjee, Temporal wetting property of “Micro” versus “Nano” rods of ZnO grown using the pressure dependent aqueous solution method, New J. Chem. 39 (2015) 8993–8998. https://doi.org/10.1039/c5nj01453k.

[45] H.Y. Erbil, Evaporation of pure liquid sessile and spherical suspended drops: A review, Adv. Colloid Interface Sci. 170 (2012) 67–86. https://doi.org/10.1016/j.cis.2011.12.006.